The Onset of Turbulence in Pipe Flow

Kerstin Avila, *et al.*

Science **333**, 192 (2011);
DOI: 10.1126/science.1203223

maximum modulus $|WS(s)|$ is always achieved on the boundary. See (*3*).
17. I. Lestas, G. Vinnicombe, J. Paulsson, *Nature* **467**, 174 (2010).
18. Materials and methods are available as supporting material on *Science* Online.
19. A. Ståhlberg *et al.*, *BMC Genomics* **9**, 170 (2008).
20. A. K. Poulsen, M. Ø. Petersen, L. F. Olsen, *Biophys. Chem.* **125**, 275 (2007).
21. P. A. Iglesias, B. P. Ingalls, *Control Theory and Systems Biology* (MIT Press, Cambridge, MA. 2010).
22. H. Sandberg, J. C. Delvenne, J. C. Doyle, *IEEE Trans Auto Control*, **56**, 293 (2011).
23. N. C. Martins, M. A. Dahleh, J. C. Doyle, *IEEE Trans. Automat. Contr.* **52**, 56 (2007).
24. A. D. Lander, *PLoS Biol.* **2**, e164 (2004).
25. G. Buzi, U. Topcu, J. Doyle, *Automatica*, **47**, 1123 (2011).
26. D. L. Alderson, J. C. Doyle, *IEEE Trans Syst. Man Cybernet. Part A Syst. Hum.* **40**, 839 (2010).

Acknowledgments: The authors thank H. El-Samad and J. Stewart-Ornstein at the University of California, San Francisco, for their laboratory space and assistance; N. Pierce (Ray Deshaies' lab) for the green fluorescent protein library; O. Venturelli (Richard Murray's lab) for her help; and M. Csete for helpful feedback. Microscopy was performed at the Nikon Imaging Center at UCSF. Experimental data are available in SOM. This work is supported by the NIH (award R01GM078992A) and Institute of Collaborative Biotechnologies from the U.S. Army Research Office (subaward KK4102, prime award DAAD19-03-D-0004).

Supporting Online Material
www.sciencemag.org/cgi/content/full/333/6039/187/DC1
Materials and Methods
SOM Text
Figs. S1 to S10
Tables S1 and S23
References (*27–31*)

22 November 2010; accepted 2 May 2011
10.1126/science.1200705

The Onset of Turbulence in Pipe Flow

Kerstin Avila,[1]* David Moxey,[2] Alberto de Lozar,[1] Marc Avila,[1] Dwight Barkley,[2,3] Björn Hof[1]*

Shear flows undergo a sudden transition from laminar to turbulent motion as the velocity increases, and the onset of turbulence radically changes transport efficiency and mixing properties. Even for the well-studied case of pipe flow, it has not been possible to determine at what Reynolds number the motion will be either persistently turbulent or ultimately laminar. We show that in pipes, turbulence that is transient at low Reynolds numbers becomes sustained at a distinct critical point. Through extensive experiments and computer simulations, we were able to identify and characterize the processes ultimately responsible for sustaining turbulence. In contrast to the classical Landau-Ruelle-Takens view that turbulence arises from an increase in the temporal complexity of fluid motion, here, spatial proliferation of chaotic domains is the decisive process and intrinsic to the nature of fluid turbulence.

The seemingly simple question as to when the flow down an ordinary pipe turns turbulent dates back to the pioneering study of Osborne Reynolds in the late 19th century (*1*). Reynolds proposed that below a critical velocity, pipe flows are always laminar, whereas above that critical velocity turbulence prevails, given the right initial conditions. The observation that this critical point can be expressed in a dimensionless form was the basis of one of the central concepts in fluid dynamics: the Reynolds number ($Re = UD/\nu$, where U is the mean velocity, D is the pipe diameter, and ν is the kinematic viscosity). Curiously, although Reynolds similarity has proved to be valid throughout fluid mechanics the value of the critical point in pipe flow has been debated ever since. In an early attempt to determine its value (*2*), Reynolds rewrote the equations of motion, separating quantities into average and fluctuating parts—a method that is now called the Reynolds decomposition. This contribution is generally regarded as the foundation of modern turbulence research, but it has failed to clarify the value of the critical point in pipe flow. Values reported in contemporary textbooks and journal papers vary widely, typically ranging from 1700 to 2300 (*3–5*), and occasionally even values in excess of 3000 (*6*) are quoted.

One circumstance that complicates this problem is that laminar pipe flow is stable to infinitesimal perturbations (*7*, *8*), and therefore in order to trigger turbulence, a disturbance of finite amplitude is required (*1*, *3*, *9*). What makes matters even more difficult is that at low Re, turbulence is transient. Here, turbulence occurs in the form of localized patches called puffs (*10*) that are embedded in the surrounding laminar flow and decay according to a memoryless process (that is, independent of their previous history) (*11*). The rapid increase in lifetime with Re has led to various proposed values for a critical point at which the lifetime would diverge and turbulence would become sustained (*4*, *12*, *13*). However, more detailed studies (*14–18*) have shown that the lifetime of individual puffs remains finite and only approaches infinity asymptotically with Re. Qualitatively, this behavior is reminiscent of the dynamics of a class of model systems called coupled map lattices (*19*). Here, individual lattice points can exhibit transient chaotic dynamics but eventually settle to a stable laminar fixed point. Because of the spatial coupling, these systems exhibit a statistical phase transition as the control parameter is increased. Below the critical point, eventually all sites will end up in the laminar phase, whereas above there is always a nonzero fraction of chaotic sites, and with increasing control parameter the fraction of laminar (nonchaotic) sites quickly diminishes. Analogies to fluid flows have been pointed out in a number of studies (*20–23*) that indicate the potential relevance of the spatial dynamics for the long-term behavior in fluid systems. In a numerical study of pipe flow, Moxey and Barkley (*24*) observed that at $Re \approx 2300$ turbulent puffs delocalize, and the turbulent fraction increases, which is in qualitative agreement with this picture. However, the stochastic nature of the spatial coupling was not taken into account, and the extremely long time-scales intrinsic to the flow could not be resolved in the simulations. In this work, we determined the critical point in pipe flow and quantified the relevant process sustaining turbulence in linearly stable shear flows.

Long-pipe experiments. Determining the point at which the proliferation of turbulence outweighs its decay and turbulence eventually becomes sustained requires that the time scales of both decay and spreading processes be captured. Because turbulent puffs move downstream at approximately the mean flow velocity, a long pipe is required to observe long time-scales. Using a precision glass tube with a relatively small diameter ($D = 4 \pm 0.01$ mm) and overall length of 15 m, a total dimensionless length of $3750D$ is achieved. The pipe is composed of 14 sections joined by machined perspex connectors that provide an accurate fit. A smooth inlet together with careful alignment of the individual pipe sections allows the flow to remain laminar up to $Re = 4400$. Deviations in Re were kept below ±5 throughout each set of measurements, which extended over periods of up to 45 hours. This precision was achieved with stringent control of both the pressure difference driving the flow and the fluid (water) temperature (±0.05 K). A detailed description of the experimental setup can be found in (*16*).

Starting from a fully developed laminar flow allows us to induce turbulence in a controlled manner and quantify the spreading rate at some downstream position. The experimental procedure is to create a single turbulent puff close to the pipe inlet and to monitor any changes in the turbulent fraction at downstream positions. It is important that a perturbation is chosen that efficiently triggers turbulence. In many earlier studies, such as (*10*, *25*), turbulence was induced by insertion of a static obstacle close to the pipe inlet. Such obstacles provide a continuous perturbation, and at high Reynolds numbers the flow downstream is fully turbulent, whereas in the transitional

[1]Max Planck Institute for Dynamics and Self-Organization, Bunsenstrasse 10, 37073 Göttingen, Germany. [2]Department of Mathematics, University of Warwick, Coventry CV4 7AL, UK. [3]Physique et Mécanique des Milieux Hétérogènes, UMR 7636 CNRS–École Supérieure de Physique et de Chimie Industrielles de la Ville de Paris–Univ Paris 06–Univ Paris 07, 10 rue Vauquelin, 75005 Paris, France.

*To whom correspondence should be addressed. E-mail: kavila@ds.mpg.de (K.A.); bhof@ds.mpg.de (B.H.)

regime ($Re \lesssim 3000$) irregular sequences of turbulent and laminar phases are created (*25*). However, at lower Reynolds numbers ($Re \approx 2000$) sufficiently strong continuous perturbations cause plug-shaped velocity profiles that are unable to sustain turbulence (*26*) and lead to relaminarization. Hence, for large disturbance levels continuous perturbations may fail to trigger turbulence at low Reynolds numbers. To avoid such problems, in the present study an impulsive perturbation was chosen, consisting of a water jet injected through a circular hole of $0.2D$ in the pipe wall $250D$ downstream of the inlet. The duration of the perturbation was adjusted for each set of measurements (8 to 20 ms, corresponding to advection of approximately 1 to $2.5D$ at the mean flow velocity), ensuring that only one single puff was generated from each perturbation. Different amplitudes were tested, and the results were found to be independent of the perturbation strength. In relation to the mass flow in the pipe, typical injection rates were about 2.5%. To establish that results were independent of the perturbation, additional measurements were carried out by using an obstacle to impulsively disturb the flow. A thin wire (0.8 mm in diameter and 10 mm in length) was inserted into the pipe $150D$ from the inlet. The wire was held against the pipe wall and aligned with the pipe axis by using a small magnet attached to the outside of the pipe. When against the wall, the disturbance created by the wire is too small to trigger turbulence for the *Re* investigated. When the wire was moved azimuthally along the pipe wall by approximately 0.5 to 1 mm in a time interval of about 0.1 s (corresponding to advection of about $10D$, based on the mean flow speed), a single turbulent puff was triggered.

After triggering disturbances, the flow was monitored by two downstream pressure sensors (fig. S1). The first one, located $300D$ from the inlet, confirmed that each perturbation results in the creation of a single puff. The second one, which can be positioned at various distances L from the perturbation, was used to distinguish cases in which multiple puffs arrive (Fig. 1A) from those in which only the single puff arrives (Fig. 1B) or no puff arrives. This is a direct measurement of whether the turbulent fraction in the flow has increased, remained constant, or decreased during downstream propagation.

Simulations. To complement experiments and gain insights into the underlying spread of turbulence, we have carried out extensive numerical simulations. Two independent numerical codes have been used; one is a spectral-element Fourier code (*27*) that solves the Navier-Stokes equations in Cartesian coordinates (DNS1), and the other is a hybrid spectral finite-difference

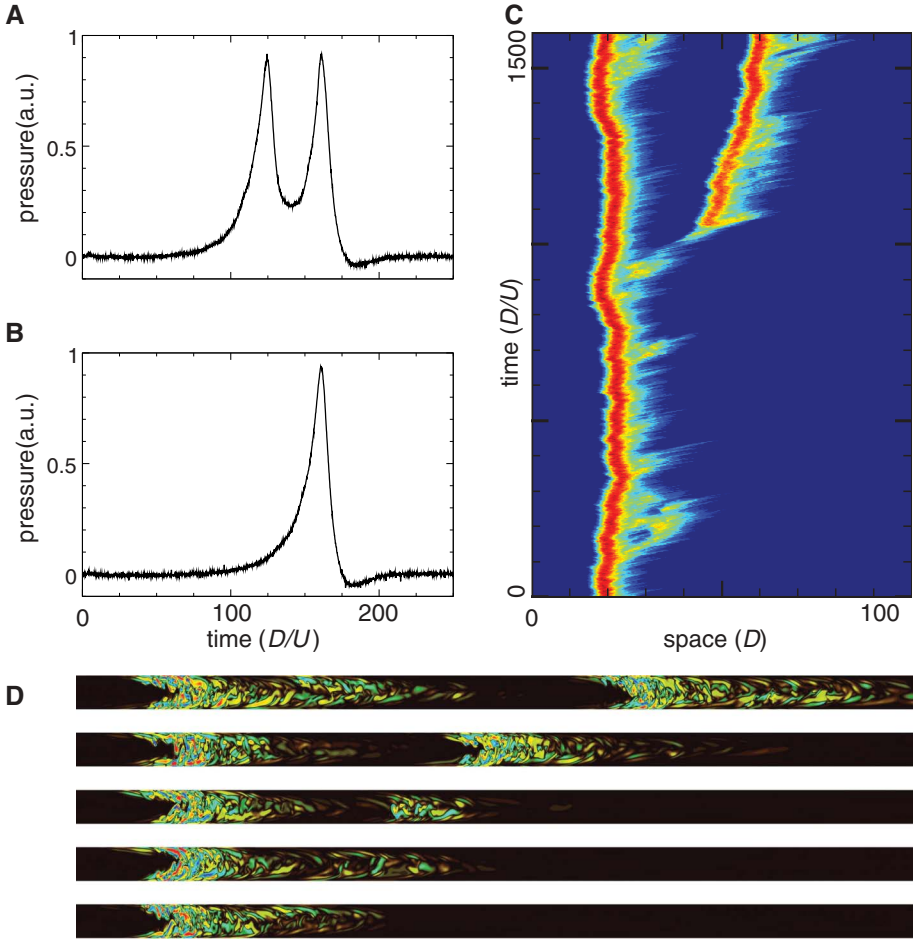

Fig. 1. Puff splitting in experiment and numerical simulation. (**A** and **B**) Pressure signals from the experiment are used to distinguish the case of (A) a split puff from (B) a single puff. A splitting is registered if the signal has peaks separated by $20D$ or more and if between peaks the signal drops by at least 30%. The flow between the two puffs does not recover to the fully developed laminar profile. (**C**) Space-time diagram from numerical simulation using the hybrid spectral finite-difference code (DNS2) at $Re = 2300$ showing the splitting process. The square of the cross-sectional average of streamwise vorticity is plotted on a logarithmic scale in a co-moving reference frame (speed $U_p = 0.929U$) and $100D$ of the $150D$ simulation domain are shown. The upstream edge of a puff is relatively well defined, whereas the downstream edge is fuzzy and fluctuates. After a splitting, the two puffs propagate downstream, separated by an approximately constant distance, and generate a twin-peaked pressure signal (A). (**D**) Visualization of puff splitting in a cross-sectional (x, y) plane, with red as positive and blue as negative streamwise vorticity on a linear scale, from the same run as (C) and showing $75D$. At $t = 0$, *Re* is impulsively changed from 2200 to 2300. Snapshots (from bottom to top) were taken at $t = 500$, 990, 1010, 1110, and 1600. Once the puff extends far enough and the vorticity decays in its central section, a new puff emerges.

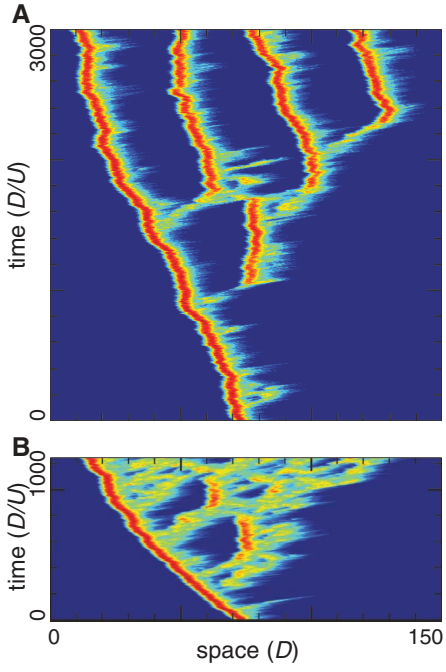

Fig. 2. Spreading of turbulence in numerical simulation. Space-time diagram at (**A**) $Re = 2300$ and (**B**) $Re = 2450$ from numerical simulation (DNS2), showing how turbulence proliferates starting from a localized puff at $Re = 2200$ as initial condition. The cross-sectional average of streamwise vorticity squared is plotted on a logarithmic scale in a co-moving reference frame at speed $0.947U$ and $0.94U$, respectively. At $Re = 2300$, the expansion process is dominated by discrete steps, corresponding to puff splits, whereas at $Re = 2450$, expansion is more smooth, more rapid, and individual puffs are no longer easily identified.

code (*28*) that solves the equations in cylindrical coordinates (DNS2). Both methods use periodic boundary conditions in the streamwise direction and impose constant unit mass flux, ensuring no variation in *Re* during any run. The codes have been tested both against each other, producing statistically identical results, and by increasing the resolution of the discretizations. Details have been reported elsewhere (*27*–*29*).

Puff splitting. For all of the lower *Re* under investigation, an increase in the turbulent fraction manifests itself in the form of "puff splitting" (*10*, *30*), in which new puffs are seeded downstream of existing ones (Fig. 1, C and D). Directly downstream of a turbulent puff, the flow has not recovered a parabolic profile and cannot sustain turbulence (*26*). To successfully seed a new puff, a patch of vorticity has to escape far enough downstream from the initial puff to an area where the velocity profile is sufficiently parabolic. This process can be observed in Fig. 1C, where regions of large vorticity fluctuations repeatedly propagate downstream and decay. Only during a sufficiently large excursion does a new puff arise downstream of the old one. Starting from a single puff, turbulence proliferates through a sequence of splittings at $Re = 2300$, as illustrated in Fig. 2A. For $Re \leq 2300$ for all of our measurements (numerical as well as experimental), spreading of turbulence and hence any increase in turbulence fraction (fig. S5) was exclusively observed in the form of puff splitting. Only at Reynolds numbers somewhat larger than considered here ($Re > 2400$) do individual puffs start to noticeably expand (Fig. 2B) so that the overall spreading of turbulence becomes a complex mixture of splitting, as well as growth and merging of individual turbulent domains.

Characteristic time of memoryless process. Because of the stochastic nature of the splitting process, a statistical approach must be used. To collect splitting statistics, we performed ensembles of numerical simulations starting from independent puffs (table S3), from which we determined the time for each to split. We let $P(Re,t)$ denote the probability that a puff at Reynolds number *Re* splits before time *t*. Then $1 - P(Re,t)$ is the probability for a puff to remain a single turbulent patch—not split, after time *t* at Reynolds number *Re*. As shown in Fig. 3, $1 - P(Re, t) = \exp[-(t - t_0)/\tau(Re)]$, where *t* is the observation time, t_0 is a formation time, and $\tau(Re)$ is the *Re*-dependent characteristic time for the process. The formation time t_0 includes any equilibration time for the initial condition to evolve to the turbulence state at the particular *Re* and the intrinsic time needed for splitting. An offset time t_0 arises in puff decay distributions for analogous reasons (*14*, *17*, *31*). In principle, t_0 depends on *Re*, as well as on the initial conditions used in ensemble runs, but from the two detailed cases in Fig. 3, as well as from the time of first splitting at other *Re*, we find consistently that $100 \leq t_0 \leq 200$.

Experimental measurements (Fig. 3, circles and squares) also reveal exponential distributions. Observations were carried out at different distances *L*, which were translated into observation time by $t = L/U_p$, where $U_p = 1.482 \times 10^{-4} - 2.416 \times 10^{-4}\, Re$ is an approximation to the mean puff speed in this *Re* range, as obtained through numerical simulation (fig. S2). Beyond the initial formation time, distributions are exponential and hence memoryless, reflecting that the probability of splitting does not depend on the age of the puff under investigation. The splitting probability is constant in time and characterized solely by τ, which after the initial formation time gives the mean time for a puff to split and the turbulence fraction to increase.

Experimentally, it is far easier to keep the observation point fixed during one series of measurement and vary *Re* in order to determine $P(Re, t)$, from which $\tau(Re)$ can be obtained. The results for five distances *L* are shown in Fig. 4. For each data point, typically 2000 measurements were performed, but for the lowest *Re*, up to 60,000 measurements were used. As expected, at large *Re* the splitting probability is high and decreases as *Re* is reduced. Curves for fixed *L* are S-shaped, indicating that $P \to 0$ only asymptotically as *Re* decreases. All measurements were well approximated by a single superexponential fit with only two parameters, $\tau = \exp[\exp(aRe + b)]$, where $a = -0.003115$ and $b = 9.161$ (Fig. 4, solid lines). In contrast to earlier studies (*10*, *24*, *30*), our data indicate that there is no critical point at which the spatial proliferation of turbulence abruptly sets in. The tendency to split appears to be intrinsic to turbulence even at low Reynolds numbers, and turbulent patches are not in an equilibrium state (*32*). It is hence the stochastic details of this process that decide whether turbulence will either spread or recede and eventually decay.

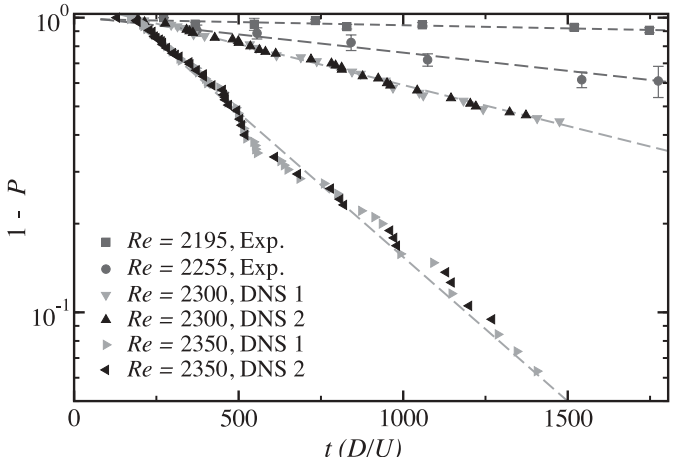

Fig. 3. Probability distributions for a puff to remain in equilibrium. *P* is the probability that a puff will split before time *t*. Hence, the plotted quantity $1 - P$ is the probability that a puff remains a single localized puff up to time *t*. The numerical distributions at $Re = 2300$ and $Re = 2350$ are obtained from all first-splitting times in ensembles of simulations by using both the spectral-element Fourier code (DNS1) and the hybrid spectral finite-difference code (DNS2). Experimental distributions at $Re = 2195$ and $Re = 2255$ are obtained from statistics collected from fixed downstream locations *L* converted to time by the *Re*-dependent mean puff propagation speed U_p. All distributions are of the form $\exp[-(t - t_0)/\tau]$, as illustrated by the dashed lines, where t_0 is a development time for splitting to take place ($t_0 \approx 150$ for DNS, whereas for the experiment, t_0 is nearer to 100 and has greater uncertainty). The exponential form of the distributions indicates that splitting is a memoryless process with characteristic time τ.

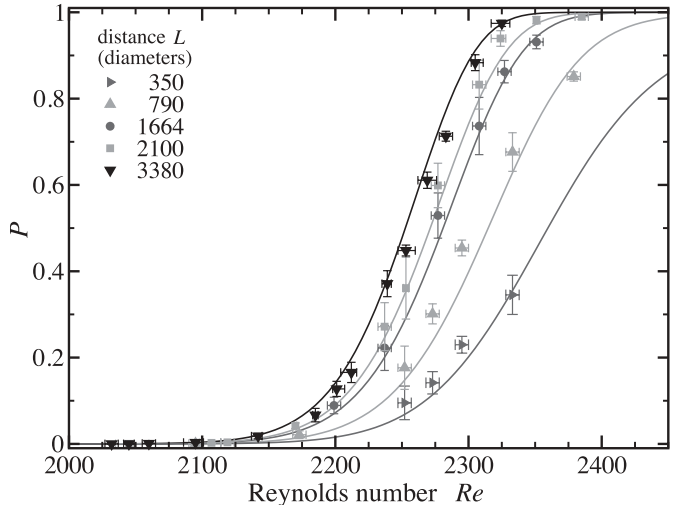

Fig. 4. Probability of puff splitting after traveling a fixed distance. The five data sets correspond to distances *L* in the experiments, as indicated in the legend. Here, the splitting probability *P* is computed as $P = r/n$, where *r* is the number of events that split and *n* is the total number of realizations. The error bars in the vertical direction are 95% confidence intervals for the parameter *P* of a binomial distribution as a function of (n, r) obtained with the Wilson method (*40*), whereas in the horizontal direction they show the uncertainty in *Re* during a set of measurements. The solid lines correspond to the superexponential fit from Fig. 5 without additional fitting parameters.

Critical point. To determine the critical point for the onset of sustained turbulence, we compared the time scale for turbulence to spread with the time scale for turbulence to decay. The dependence of the mean splitting time on *Re* is plotted in Fig. 5. From each experimental data point in Fig. 4, the mean time τ was obtained and plotted (Fig. 5, right branch, colored symbols), together with the single superexponential fit (Fig. 5, solid line). In order to obtain τ from the experimental probabilities, a formation time of $t_0 = 100$ was considered [uncertainties in $t_0 = (50,150)$ are included in the error bars]. Because in experiments observation times are generally large, the uncertainties in t_0 are negligible compared with statistical errors.

Additionally, τ values from simulations are included in Fig. 5 (black solid triangles), showing that results from both numerical codes are in excellent agreement with the experimental data. From ensemble simulations, we can obtain directly the times for each split and a maximum likelihood estimate of τ from the memoryless character of the splitting process (*17*, *33*). The rapid increase in splitting times makes it infeasible to obtain τ numerically at low *Re*.

The left branch in Fig. 5 summarizes previously measured mean lifetimes for turbulent decay (*15*, *17*, *18*), together with a single superexponential fit for mean lifetimes. The intersection at $Re \approx 2040$ marks where the mean lifetime is equal to the mean splitting time, and to the right of the intersection, splittings outweigh the decay of puffs. Analyzing the data in terms of the turbulent fraction results in the same critical point (fig. S5), confirming the procedure applied here.

Typically in statistical phase transitions, critical points are not identical to the exact balance point of two competing processes because of correlations. For example, in the standard contact process (*34*, *35*) the spreading (contamination) rate of an active phase has to outweigh its decay (recovery) rate by a ratio of about 3 before the active phase becomes sustained. Although in the present case the long time scales make it impossible to measure other signatures of criticality such as scale invariance, the superexponential scaling of the two processes ensures that the critical point will be almost indistinguishable from the intersection point. For an increase in *Re* of 10 (or 0.5%) above the critical point, the splitting rate already outweighs the decay rate by a factor of 4. Therefore, the difference between the intersection point and the critical point is of the same order as the experimental uncertainty in *Re*, and 2040 ± 10 provides a close estimate of the critical point for the onset of sustained turbulence.

Conclusion. The complexity of the transition process encountered in pipe flow is common to many shear flows, including Couette, channel, duct, and boundary layer flows. In all of these flows, turbulence is found despite the stability of the base flow and first takes the form of localized patches, which are transient. The key to the approach here to determine the onset and sustainment of turbulence has been to separate the analysis of decay and proliferation mechanisms, and this approach should be equally applicable even though details of these mechanisms may differ from case to case. In all of these flows (analogous to our findings for pipe flow), the spatial coupling of transiently chaotic domains may give rise to the sustainment of turbulence (*23*), breaking with the classical view that turbulence arises through an increase in temporal complexity (*36*, *37*). The intermittently alternating laminar and turbulent regions encountered in pipe flow just above criticality are intrinsic to the problem and place pipe flow in the larger theoretical framework of spatiotemporal intermittency (*19*, *38*) and nonequilibrium phase transitions in which universal scaling properties may be expected (*20*, *35*, *39*). Although in the present study the spatial interaction is relatively simple because of the clear separation of adjacent puffs, further above the critical point ($Re \gtrsim 2400$) the dynamics quickly become increasingly complicated, with domains merging and annihilating. To comprehend this increasing spatial complexity is a challenge for future studies and is key to our understanding the onset and nature of turbulence.

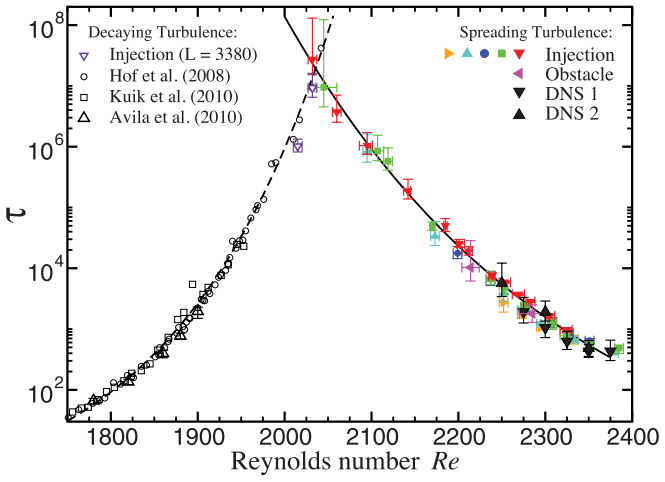

Fig. 5. Mean lifetime of a puff before decaying or splitting. Solid colored symbols correspond to experimental splitting measurements. Measurements downstream of jet injection are at different distances *L* as indicated in Fig. 4. Measurements downstream of an obstacle perturbation are at *L* = 1700. The solid black triangles show the characteristic splitting time obtained from direct numerical simulations using the spectral-element Fourier code (DNS1) and the hybrid spectral finite-difference code (DNS2). The solid curve is given by $\tau = \exp[\exp(-0.003115\,Re + 9.161)]$ and approximates the *Re*-dependence of mean time until a second puff is nucleated and the turbulent fraction increases. This curve was obtained by fitting the data sets with distances *L* = 1664, 2100, and 3380, whereas results from shorter pipes were not fitted because of the stronger influence of the uncertainty in t_0. The dashed curve is given by $\tau = \exp[\exp(0.005556\,Re - 8.499)]$ and approximates the *Re*-dependence of the mean time until turbulence decays and the flow relaminarizes. Both curves correspond to superexponential scaling with *Re* and have a crossover at $Re = 2040 \pm 10$, determining the transition between transient and sustained turbulence in pipe flow in the thermodynamic limit.

References and Notes

1. O. Reynolds, *Philos. Trans. R. Soc. London Ser. A* **174**, 935 (1883).
2. O. Reynolds, *Philos. Trans. R. Soc. London Ser. A* **186**, 123 (1895).
3. A. Darbyshire, T. Mullin, *J. Fluid Mech.* **289**, 83 (1995).
4. H. Faisst, B. Eckhardt, *J. Fluid Mech.* **504**, 343 (2004).
5. B. Eckhardt, *Philos. Trans. R. Soc. London Ser. A* **367**, 449 (2009).
6. B. Eckhardt, *Nonlinearity* **21**, T1 (2008).
7. P. Drazin, W. Reid, *Hydrodynamic Stability* (Cambridge Univ. Press, Cambridge, 2004).
8. A. Meseguer, L. Trefethen, *J. Comput. Phys.* **186**, 178 (2003).
9. B. Hof, A. Juel, T. Mullin, *Phys. Rev. Lett.* **91**, 244502 (2003).
10. I. J. Wygnanski, F. H. Champagne, *J. Fluid Mech.* **59**, 281 (1973).
11. B. Eckhardt, T. M. Schneider, B. Hof, J. Westerweel, *Annu. Rev. Fluid Mech.* **39**, 447 (2007).
12. A. P. Willis, R. R. Kerswell, *Phys. Rev. Lett.* **98**, 014501 (2007).
13. J. Peixinho, T. Mullin, *Phys. Rev. Lett.* **96**, 094501 (2006).
14. B. Hof, J. Westerweel, T. M. Schneider, B. Eckhardt, *Nature* **443**, 59 (2006).
15. B. Hof, A. de Lozar, D. J. Kuik, J. Westerweel, *Phys. Rev. Lett.* **101**, 214501 (2008).
16. A. de Lozar, B. Hof, *Philos. Trans. R. Soc. London Ser. A* **367**, 589 (2009).
17. M. Avila, A. Willis, B. Hof, *J. Fluid Mech.* **646**, 127 (2010).
18. D. Kuik, C. Poelma, J. Westerweel, *J. Fluid Mech.* **645**, 529 (2010).
19. K. Kaneko, *Prog. Theor. Phys.* **74**, 1033 (1985).
20. Y. Pomeau, *Physica D* **23**, 3 (1986).
21. S. Bottin, H. Chaté, *Eur. Phys. J. B* **6**, 143 (1998).
22. S. Bottin, F. Daviaud, P. Manneville, O. Dauchot, *Europhys. Lett.* **43**, 171 (1998).
23. P. Manneville, *Phys. Rev. E Stat. Nonlin. Soft Matter Phys.* **79**, 25301 (2009).
24. D. Moxey, D. Barkley, *Proc. Natl. Acad. Sci. U.S.A.* **107**, 8091 (2010).
25. J. Rotta, *Arch. Appl. Mech.* **24**, 258 (1956).
26. B. Hof, A. de Lozar, M. Avila, X. Tu, T. M. Schneider, *Science* **327**, 1491 (2010).
27. H. M. Blackburn, S. J. Sherwin, *J. Comput. Phys.* **197**, 759 (2004).
28. A. P. Willis, R. R. Kerswell, *J. Fluid Mech.* **619**, 213 (2009).
29. Materials and methods are available as supporting material on *Science* Online.
30. M. Nishi, B. Ünsal, F. Durst, G. Biswas, *J. Fluid Mech.* **614**, 425 (2008).
31. T. M. Schneider, B. Eckhardt, *Phys. Rev. E Stat. Nonlin. Soft Matter Phys.* **78**, 046310 (2008).
32. I. Wygnanski, M. Sokolov, D. Friedman, *J. Fluid Mech.* **69**, 283 (1975).
33. J. Lawless, *Statistical Models and Methods for Lifetime Data* (Wiley, New Jersey, ed. 2, 2003).
34. T. Harris, *Ann. Probab.* **2**, 969 (1974).
35. H. Hinrichsen, *Adv. Phys.* **49**, 815 (2000).

36. L. Landau, E. Lifshitz, *Fluid Mechanics*, vol. 225 (Pergamom, New York, 1959).
37. D. Ruelle, F. Takens, *Commun. Math. Phys.* **20**, 167 (1971).
38. H. Chaté, P. Manneville, *Physica D* **32**, 409 (1988).
39. J. Rolf, T. Bohr, M. Jensen, *Phys. Rev. E Stat. Phys. Plasmas Fluids Relat. Interdiscip. Topics* **57**, R2503 (1998).
40. L. D. Brown, T. T. Cai, A. DasGupta, *Stat. Sci.* **16**, 101 (2001).

Acknowledgments: We thank A. P. Willis for sharing his hybrid spectral finite-difference code. We acknowledge the Deutsche Forschungsgemeinschaft (project FOR 1182), the Max Planck Society, and the Engineering and Physical Sciences Research Council (grant EP/F017413/2) for financial support. D.B. thanks the Leverhulme Trust and the Royal Society for their support. M.A. and B.H. acknowledge computing resources from GWDG (Gesellschaft für wissenschaftliche Datenverarbeitung Göttingen) and the Jülich Supercomputing Centre (grant HGU16), where DNS2 were performed. D.M. and D.B. acknowledge computing resources from the Centre for Scientific Computing, University of Warwick, and Grand Equipement National de Calcul Intensif-Institut du Développement et des Ressources en Informatique Scientifique (grants 2010-1119 and 2011-1119), where DNS1 were performed. K.A. acknowledges support from the International Max Planck Research School for the Physics of Biological and Complex Systems and the Göttinger Graduate School for Neurosciences and Molecular Biosciences.

Supporting Online Material

www.sciencemag.org/cgi/content/full/333/6039/192/DC1
Materials and Methods
Figs. S1 to S5
Tables S1 to S3
References

24 January 2011; accepted 19 May 2011
10.1126/science.1203223

REPORTS

Frequency Metrology in Quantum Degenerate Helium: Direct Measurement of the $2\,^3S_1 \rightarrow 2\,^1S_0$ Transition

R. van Rooij,[1] J. S. Borbely,[1] J. Simonet,[2] M. D. Hoogerland,[3] K. S. E. Eikema,[1] R. A. Rozendaal,[1] W. Vassen[1]*

Precision spectroscopy of simple atomic systems has refined our understanding of the fundamental laws of quantum physics. In particular, helium spectroscopy has played a crucial role in describing two-electron interactions, determining the fine-structure constant and extracting the size of the helium nucleus. Here we present a measurement of the doubly forbidden 1557-nanometer transition connecting the two metastable states of helium (the lowest energy triplet state $2\,^3S_1$ and first excited singlet state $2\,^1S_0$), for which quantum electrodynamic and nuclear size effects are very strong. This transition is weaker by 14 orders of magnitude than the most predominantly measured transition in helium. Ultracold, submicrokelvin, fermionic ^{3}He and bosonic ^{4}He atoms are used to obtain a precision of 8×10^{-12}, providing a stringent test of two-electron quantum electrodynamic theory and of nuclear few-body theory.

The first observations of helium emission spectra at the end of the 19th century revealed two separate series of lines, associated with orthohelium and parahelium, respectively. In 1926, Heisenberg explained the distinction between these two spectra on the basis of wave mechanics, electron spin, and the Pauli exclusion principle (*1*). The spectrum of orthohelium arises from triplet states for which the electron spins are parallel, whereas in parahelium the electron spins are antiparallel, forming singlet states (Fig. 1). From the lowest state of orthohelium, the 1s2s $^3S_1$ state (denoted $2\,^3S_1$), only excitations to triplet states have been observed. Orthohelium transitions from the $2\,^3S_1$ state and associated studies of the $n\,^3P_{0,1,2}$ (n = 2,3) fine-structure splittings (*2*–*7*) have enabled tests of quantum electrodynamics (QED) (*8*, *9*), as well as a determination of the fine-structure constant (*5*, *10*). In the singlet spectrum of helium (parahelium), electric-dipole transitions from the $1\,^1S_0$ ground state (*11*) and from the metastable $2\,^1S_0$ state (*12*, *13*) have also provided tests of high-precision QED calculations. All these frequency metrology studies have been performed using either atomic beams or gas discharges. However, helium in the metastable $2\,^3S_1$ state (He*, lifetime 8×10^3 s) can be laser-cooled and trapped, which allows much longer interaction times for excitation of weak transitions. He* atoms have been cooled to μK temperatures, which revealed quantum statistical effects of bunching and antibunching (*14*) and allowed quantum degeneracy to be achieved for both the bosonic isotope ^{4}He (*15*, *16*) and the fermionic isotope ^{3}He (*17*).

Here we observe an orthohelium-parahelium transition, specifically, the 1557-nm transition between the metastable $2\,^3S_1$ and $2\,^1S_0$ states (Fig. 1), both in ^{4}He and ^{3}He. This transition is an excellent testing ground for fundamental theory of atomic structure. Because of a large electron density at the nucleus, the energy of S states is the most sensitive to QED and to nuclear size effects (*8*). For the $2\,^3S_1$ and $2\,^1S_0$ metastable states, QED terms contribute 4 and 3 GHz respectively, to a total binding energy of 10^6 GHz (*8*, *9*). The present accuracy in the QED calculations is 2 MHz, based on an estimate of non-evaluated higher-order terms. Many of these terms are common between the isotopes. Therefore, in the calculation of the isotope shift (i.e., the difference between the transition frequencies for ^{4}He and ^{3}He), mass-independent terms cancel, and the uncertainty is reduced to the sub-kHz level (*18*). As the finite nuclear charge radius shifts the $2\,^3S_1$ state by 2.6 MHz and the $2\,^1S_0$ state by 2.0 MHz, an accurate isotope-shift measurement allows a sensitive determination of the difference in the mean charge radius of the α particle and of the ^{3}He nucleus, which provides a stringent test of nuclear charge radius calculations and experiments (*19*).

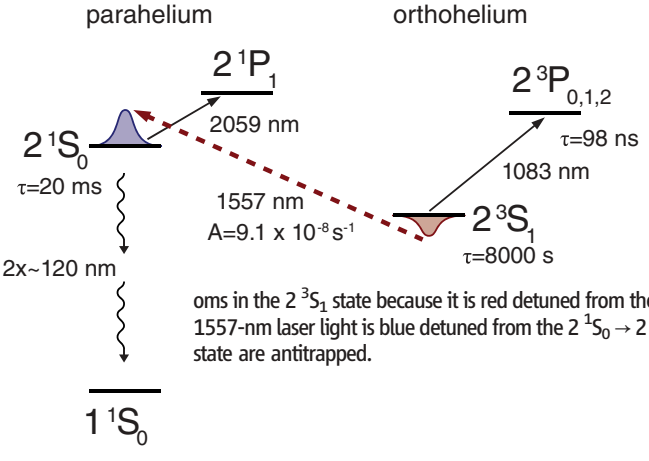

Fig. 1. Relevant energy levels, transition wavelengths, and state lifetimes of helium. The magnetic-dipole transition connecting the $2\,^3S_1$ state and the $2\,^1S_0$ state has a wavelength of 1557 nm and an Einstein A coefficient of 9.1×10^{-8} s^{-1}. A focused 1557-nm laser also constitutes a trap for ultracold atoms in the $2\,^3S_1$ state because it is red detuned from the $2\,^3S_1 \rightarrow 2\,^3P_J$ transitions. As the 1557-nm laser light is blue detuned from the $2\,^1S_0 \rightarrow 2\,^1P_1$ transition, atoms in the $2\,^1S_0$ state are antitrapped.

[1]LaserLaB Vrije Universiteit, De Boelelaan 1081, 1081 HV Amsterdam, Netherlands. [2]École Normale Supérieure, Laboratoire Kastler-Brossel, 24 rue Lhomond, 75005 Paris, France. [3]Department of Physics, University of Auckland, Private Bag 92019, Auckland, New Zealand.

*To whom correspondence should be addressed. E-mail: w.vassen@vu.nl